Fluorescent Zr(IV) Metal–Organic Frameworks Based on an Excited-State Intramolecular Proton Transfer-Type Ligand

Virgile Trannoy, Nathalie Guillou, Carine Livage, Catherine Roch-Marchal, Mohamed Haouas, Anne Léaustic, Clémence Allain, Gilles Clavier, Pei Yu, Thomas Devic

Fluorescent Zr(IV) Metal Organic Frameworks based on an Excited state intramolecular proton transfer (ESIPT)-type ligand

Virgile Trannoy[†,‡,§]*, Nathalie Guillou[†], Carine Livage[†], Catherine Roch-Marchal[†], Mohamed Haouas[†], Anne Léaustic[‡], Clémence Allain[§], Gilles Clavier[§], Pei Yu[‡]* and Thomas Devic[‖] *

[†] ILV, Université de Versailles St Quentin, UMR CNRS 8180, Université Paris-Saclay, 78035 Versailles, France

[‡] ICMMO, Université Paris-Sud, UMR CNRS 8182, Université Paris-Saclay, 91405 Orsay Cedex, France

[§] PPSM, ENS Cachan, UMR CNRS 8531, Université Paris-Saclay, 94235 Cachan, France

[‖] Institut des Matériaux Jean Rouxel (IMN), Université de Nantes, UMR CNRS 6502, 2 rue de la Houssinière, BP 32229, 44322 Nantes cedex 3, France

KEYWORDS: Metal-Organic Frameworks, Fluorescence, ESIPT, Zirconium, Structure analysis, Stability

ABSTRACT: We report here the preparation of a series of Zr(IV) Metal Organic Frameworks of the MIL-140 structure type incorporating a ligand exhibiting an intense Excited State Intramolecular Proton Transfer (ESIPT) fluorescence. These solids were obtained by systematically varying the substitution rate of 4,4'-biphenyldicarboxylate by 2,2'-bipyridine-3,3'-diol-5,5'-dicarboxylate, and thoroughly characterized by complementary techniques, including high resolution powder X-ray diffraction, solid state NMR spectroscopy, nitrogen sorption experiments and time-resolved fluorescence. We showed that the incorporation of the ESIPT-type ligand induces an increase of the hydrophilicity, leading ultimately to a higher sensitivity toward hydrolysis, a phenomenon rarely observed in this structure type considered as one of the most stable among the Zr carboxylate MOFs. Eventually, the optimization of the amount of fluorescent ligand within the structure allowed combining a decent microposity (S_{BET} > 750 $m^2.g^{-1}$) and a high stability even in boiling water, together with a high fluorescence quantum yield (> 30%).

INTRODUCTION

Porous coordination polymers or Metal-Organic Frameworks (MOFs), with their wide variety of chemical composition and structural diversity are now considered promising candidates not only for purely sorption-related applications, but also in other areas where their tunable optical or electronic properties are definite advantages. Specifically, light emitting MOFs have been proposed for optical sensing, lighting, imaging, or luminescence thermometry.[1-7] Although lanthanide-based emitters have been widely studied, organic luminophores are also appealing, especially because of their greater sensitivity to guest molecules. Nevertheless, this sensitivity is often affected by low quantum yields of fluorescence, a consequence of short luminophore-luminophore contacts leading to intra-framework quenching phenomena.[8-11] In order to create highly emissive MOFs, we have focused our attention on the use of ligands presenting an ESIPT-type fluorescence (Excited State Intramolecular Proton Transfer).[12-13]

ESIPT is an ultrafast photochemical process and its resulting emission characterized by an "abnormally" large Stokes shift and a very environment-specific sensitivity induced by the intramolecular hydrogen bond. A four-level photo-cycle (E → E* → K* → K) diagram is shown in Figure 1 to illustrate the main photochemical and photophysical processes involved in the case of an archetypal molecule of this family, the 2-(2-hydroxyphenyl)-benzothiazole (HBT). Unlike many organic emitters, self-quenching in ESIPT-type fluorophores is minimized due to the absence of spectral overlapping between absorption and emission. This unique feature of ESIPT emission is appealing for the design of efficient fluorescent materials.[12-13] ESIPT chromophores-based MOFs are thus prime candidates for potential applications in a wide variety of fields such as chemical sensors, fluorescence imaging or light emitting diodes. To date, only a very limited number of porous materials with ESIPT-type fluorescence have been reported, showing far above average fluorescent quantum yields.[2,14-23] Most of these solids are based on divalent cations (Mg, Zn, Ca, Sr, Ba) and carboxylate linkers, and are therefore prone to hydrolysis.[24]

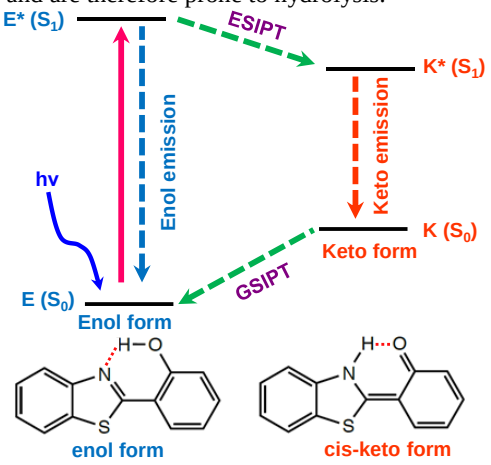

Figure 1. *Diagram of the ESIPT process. Adapted from ref [13]. Copyright 2016 The Royal Society of Chemistry.*

Group IV metal ions are well known for their strong affinity with oxygenated complexing groups, resulting in high metal-ligand bond stability toward hydrolysis.[25-27] Based on this consideration, we focused our attention on Zr(IV)-dicarboxylate MOFs. While the UiO-6n series exhibits the well-known *fcc* structure type with twelve organically linked Zr_6 oxo-clusters leading to octahedral and tetrahedral cages, the pseudo-polymorphs MIL-140s are built up from chains of edge sharing ZrO_7 polyhedra connected through the ligands to define triangular channels.[28-29] In this structure type, the organic moieties are located on two independent crystallographic sites in a 1 to 1 ratio (Figure 2). MIL-140s present lower porosities than their UiO-6n analogues, but higher chemical and mechanical stabilities.[29]

Although MIL-140 type solids are less numerous than the UiO-6n ones, the incorporation of functionalized linear ligands was already successfully achieved.[30-32] Among the MIL-140s, the one built up from the 4,4'-biphenyldicarboxylate (BPDC) and quoted MIL-140C appears as a suitable platform. In order to synthesize MIL-140C-type emitting MOFs, we focused our attention on the 2,2'-bipyridine-3,3'-diol-5,5'-dicarboxylic acid ($H_2BP(OH)_2DC$, see Scheme 1), which exhibits an intense ESIPT fluorescence in the solid state, and is analogous in size and shape to the H_2BPDC.

In this article, we report the synthesis of an ESIPT fluorescent MIL-140C series with different $BP(OH)_2DC$/BPDC ratios. Their in-depth structural characterization by combining high resolution X-ray powder diffraction (XRPD) and solid-state NMR is presented, as well as the study of their chemical stability and optical properties, with a special focus on the maximization of the quantum yield.

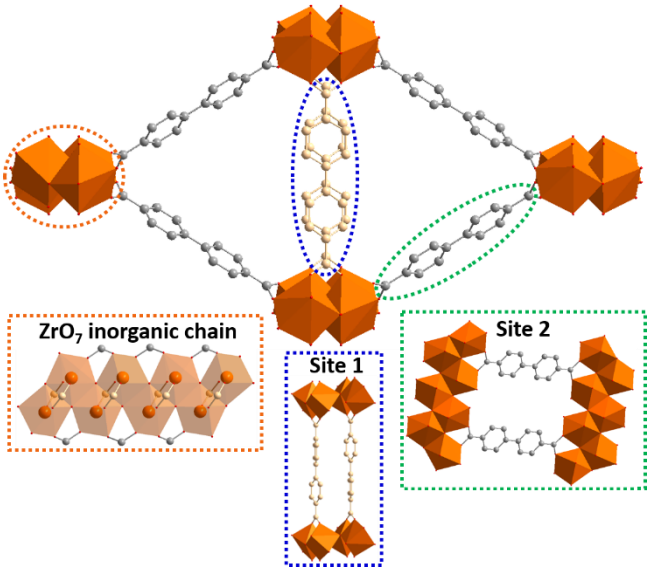

Figure 2. *Crystal structure of* ***MIL-140C_0****. Top: view along the c axis; bottom: details of the arrangement of the ligands in site 1 along the a axis (blue), and in the site 2 along the b axis (green).*

MATERIALS AND METHODS

Reagents and Chemicals. $ZrCl_4$ (anhydrous, 99.5%), acetic acid (99.7%), and *N,N'*-dimethylformamide (DMF, 99.8 %) were purchased from Sigma-Aldrich while 4,4'-biphenyldicarboxylic acid (H_2BPDC, 97 %) was purchased from ABCR. All chemicals were used without further purification. The synthesis of the ESIPT fluorophore $H_2BP(OH)_2DC$ is described in supporting information.

Synthesis of MIL-140C_n. The protocol is derived from the procedure reported by De Vos *et al.* for the preparation of MIL-140C.[33] A solution **1** of $ZrCl_4$ (233 mg, 1 mmol) in DMF (4 mL) and a solution **2** containing 1.5 mmol of dicarboxylic acid with the proper $H_2BP(OH)_2DC/H_2BPDC$ ratio (see Table S1) and glacial acetic acid (367 µL, 6.4 mmol) in DMF (6 mL) were heated at the boiling point. Solution **1** was then added to solution **2** and the mixture heated to reflux for 16 h. The white to yellow powders were recovered by centrifugation and washed with DMF. In order to remove all traces of free organic ligand from the pores, the solids were transferred to autoclaves and heated at 100°C for 14 h first in DMF, then in MeOH. The powder was recovered by centrifugation and then dried under vacuum at 80°C overnight.

CHARACTERIZATIONS

Routine X-Ray powder diffraction (XRPD) patterns were collected at room temperature on a Siemens D5000 Diffractometer working in Bragg-Brentano geometry [(θ-2θ) mode] by using CuKα radiation. The high resolution XRPD data used for the structural analysis were measured at room temperature on a Bruker D8 Advance diffractometer with a Debye-Scherrer geometry, equipped with a Ge(111) monochromator selecting Cu Kα_1 radiation (λ = 1.540598 Å) and a LynxEye detector. Powders were loaded in 0.5 mm diameter glass capillaries and dried at 100 °C overnight prior to the measurements. Data were collected in the 2θ range 4-90°. Extractions from the peak positions, pattern indexing, whole powder pattern decomposition, difference Fourier calculations and Rietveld refinements were carried out with the TOPAS program.[34]

Prior to the sorption measurements, the solids were activated under vacuum at 220 °C overnight using a BELPREP apparatus. N_2 sorption isotherms at 77 K were measured with a BELSORP Max porosimeter, and surface areas were estimated by applying the Brunauer−Emmett−Teller (BET) model.

For solid-state NMR measurements, the solids were packed in 3.2 mm zirconia rotors and the MAS spectra were recorded on a Bruker Avance 500 spectrometer at a resonance frequency of 500.1 MHz for ^{1}H, and 125.8 MHz for ^{13}C. The samples were spun at 20 kHz for the ^{1}H detection measurements and at 10 kHz for the ^{13}C detection experiments. For the ^{1}H MAS NMR spectra 8 scans were recorded with a recycle delay of 9 s and a 90° pulse of 2 µs. The ^{1}H→^{13}C cross-polarization (CP) MAS NMR spectra were recorded using a 3 ms contact time, 1.5 s recycle delay and ^{1}H SPINAL-64 decoupling. 1024 transients were accumulated. The ^{1}H–^{1}H single quantum-double quantum (SQDQ) MAS NMR spectra used the back-to-back (BABA) sequence with recoupling time ranging from 0.2 to 0.4 ms. 256 t_1 slices with 16 transients each were recorded with a recycle delay of 1 s. For the ^{1}H–^{13}C HETCOR MAS NMR spectrum, the contact time was set to 2 ms, 32 t_1 slices with 256 transients each were recorded, with recycle delay of 1 s. 2-D NMR data were recorded using the States procedure to obtain phase sensitive spectra. Tetramethylsilane was used as an external chemical shift reference for both ^{1}H and ^{13}C.

Thermogravimetric analyses (TGA) were performed on a Mettler-Toledo TGA/DSC 1 apparatus. Solids were heated up to 600 °C with a heating rate of 5°C.min^{-1} in an oxygen flow (50 mL.min^{-1}).

Fourier transform infrared (FT-IR) spectra were recorded using a Nicolet 6700 FT-IR spectrometer with a diamond attenuated total reflectance unit. The spectra were recorded from 4000 to 400 cm^{-1} with a resolution of 2 cm^{-1} at 32 scans.

Absolute fluorescent quantum yields were measured using a Fluorolog-3 from Horiba Jobin-Yvon equipped with an integrating sphere. Fluorescence decay curves were obtained by the time-correlated single-photon counting (TCSPC) method with a femtosecond laser excitation composed of a Titanium Sapphire laser (Tsunami, Spectra-Physics) pumped by a doubled Nd:YVO4 laser (Millennia Xs, Spectra-Physics). Light pulses at 800 nm from the oscillator, were selected by an acousto-optic

crystal at a repetition rate of 4 MHz, and then doubled at 400 nm by a non-linear crystal. Fluorescence photons were detected at 90° through a monochromator and a polarizer at magic angle by means of a Hamamatsu MCP R3809U photomultiplier, connected to a SPC-630 TCSPC module from Becker & Hickl. The instrumental response function was recorded before each decay measurement with a fwhm (full width at half-maximum) of ~25 ps. The fluorescence data were analyzed using the Globals software package developed at the Laboratory for Fluorescence Dynamics at the University of Illinois at Urbana-Champaign, which includes reconvolution analysis and global non-linear least-squares minimization method.

RESULTS AND DISCUSSION

Synthesis and basic characterization

$H_2BP(OH)_2DC$ (Scheme 1) was prepared from the corresponding ester at the gram scale. As expected, after excitation at 390 nm, this molecule exhibits an ESIPT-type fluorescence with an emission band centered at 562 nm and a quantum yield of 29% in the solid state (see Table 1).

Scheme 1. 2,2'-bipyridine-3,3'-diol-5,5'-dicarboxylic acid ($H_2BP(OH)_2DC$)

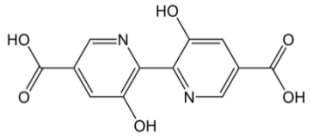

MOFs were prepared from various ratios $H_2BP(OH)_2DC/H_2BPDC$ (0/100, 10/90, 50/50 and 100/0). The resulting products, labelled **MIL-140C_0**, **MIL-140C_0.1**, **MIL-140C_0.5** and **MIL-140C_1** respectively, were first characterized by X-ray powder diffraction (XRPD). All solids present diagrams similar to that of the pristine **MIL-140C_0**, indicating that they all belong to the intended structure type (Figure 3).

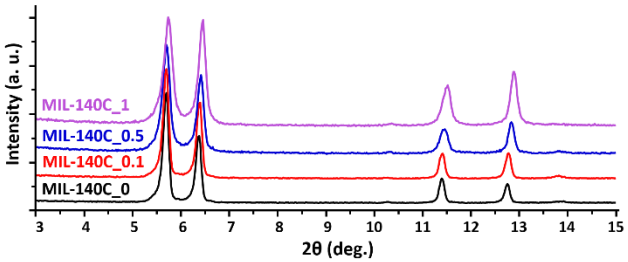

Figure 3. *XRPD of **MIL-140C_0**, **_0.1**, **_0.5** and **_1**.*

A slight shift of the Bragg peaks toward higher angles upon increasing the amount of fluorophore is observed, indicating a decrease of the unit cell volume of the solids (see Figure S6 and Table S4). As discussed later, this effect arises not only from the partial substitution of BPDC by $BP(OH)_2DC$, but also from a variable amount of water adsorbed in the pores.

Elemental analyses confirm the successful incorporation of $BP(OH)_2DC$ within the framework (see Table S2). Analysis of **MIL-140C_0.5** suggests a preferential incorporation of $BP(OH)_2DC$ over BPDC (65% of $BP(OH)_2DC$ in the final product instead of 50% in the initial reaction mixture), in agreement with the solid-state NMR analyses (see Table S3 and below). Infrared spectroscopy also corroborates the presence of the fluorophore within **MIL-140C_0.1**, **MIL-140C_0.5** and **MIL-140C_1**. Few specific bands of the $BP(OH)_2DC$ ligand, notably at 1233 and 1330 cm^{-1} (C-O elongation and O-H stretching, respectively), 1476 and 1129 cm^{-1} (elongation and deformation of the C-N bond, respectively), and at 916 and 975 cm^{-1} (aromatic γ_{C-H} bands) clearly increase with the amount of $BP(OH)_2DC$ (Figure S1). It should also be noted that almost no signal is visible in the 1700 cm^{-1} region, confirming the absence of free carboxylic acid, and hence the incorporation of $BP(OH)_2DC$ within the framework and not as a guest within the pores.

In depth structural analysis

Structural insights and quantitative information about the arrangement of the ligands within the solids were obtained from solid-state NMR analysis. ^1H MAS NMR was first used to follow specifically the proton involved in the ESIPT process (Figure 4). The spectrum of **MIL-140C_0** exhibits non-resolved resonances in the range 5-8 ppm assigned to the aromatic protons of the linker. The ^1H NMR of **MIL-140C_1** shows a more complex spectrum where beside resonances of water (4 ppm) and of OH defects in the ZrO_7 chain (1-3 ppm),[35-36] four signals are now visible for aromatic protons at 6.1, 6.7, 7.6, and 8.5 ppm in addition to two new low-field resonances at 11.8 and 13.4 ppm. Detailed decomposition of the spectra can be found in Figure S2 in Supporting Information. These particular low-field signals, between 11 and 15 ppm, are signature of deshielded protons involved in strong H-bonding and correspond to the phenol groups of the ligands engaged in the ESIPT process. The splitting of the signals of these protons and those of the aromatics with the expected 1:1 ratio is an indication of the existence of two crystallographic nonequivalent $BP(OH)_2DC$ ligands, in line with the reported structure of MIL-140s (see Figure 2). The partially substituted solids **MIL-140C_0.1** and **MIL-140C_0.5** were then studied. First, upon deconvolution of the ^1H spectra (Figure S3), the amount of BP(OH)DC was quantified. In line with the chemical analyses, a preferential incorporation of the fluorescent ligand was found both in **MIL-140C_0.1** (16%) and **MIL-140C_0.5** (65%) (see Table S3). Interestingly, the distribution of the signals characteristics of the phenol groups is no longer statistical in these solids. Indeed, at a low substitution rate (10%), a single signal is observed at 11.8 ppm. This indicates that for **MIL-140C_0.1**, the $BP(OH)_2DC$ are positioned in a preferential site. This preferential occupancy is also observed with **MIL-140C_0.5,** showing a ca 65:35 ratio between the signals at 11.8 and 13.4 ppm. The solids were further analyzed by ^{13}C MAS NMR (Figures S3 and S4). For **MIL-140C_0**, the spectrum presents two sets of resonances in the ranges 120-150 and 170-180 ppm, corresponding to aromatic and carboxylate carbons respectively.[37] Signals in the same ranges are observed for **MIL-140C_1**, but two additional resonances are also visible at 156.0 and 157.4 ppm, and attributed to the carbons bearing OH groups. As in the ^1H NMR spectra, their relative proportion evolves depending on the level of substitution, with a preferential occupancy of the site associated with the signal at 156.0 ppm.

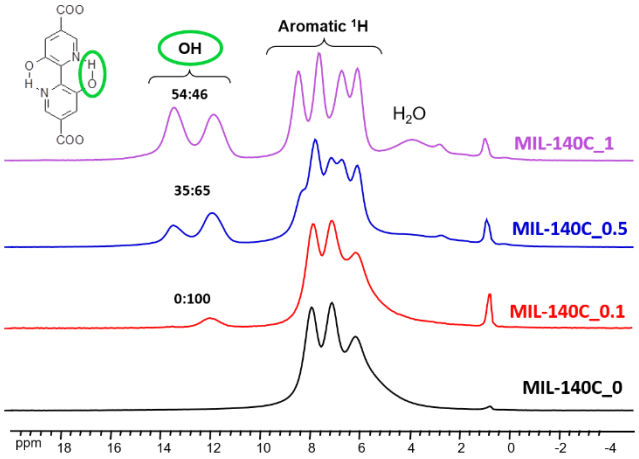

Figure 4. ^{1}H solid state NMR spectra of the MIL-140C_n series.

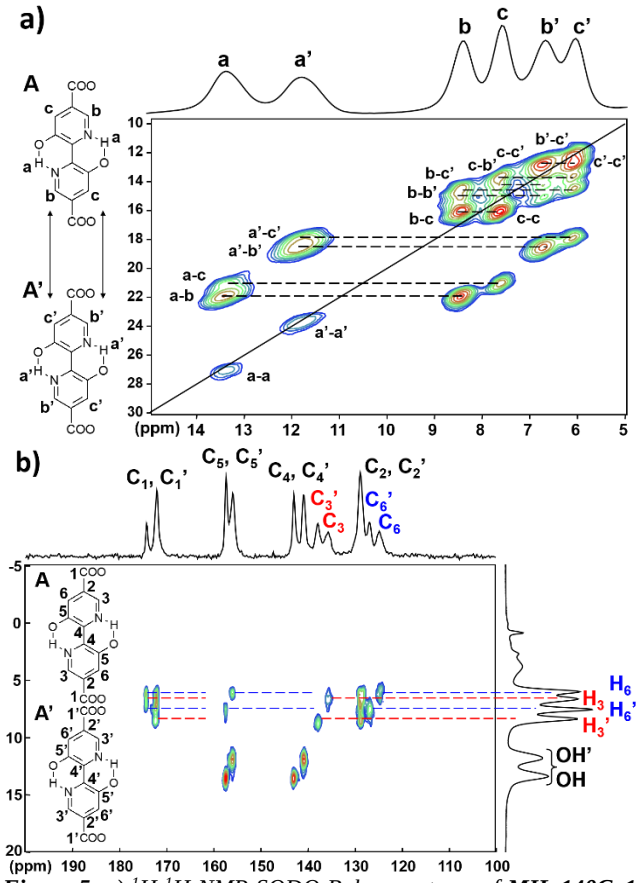

Figure 5. *a) ^{1}H-^{1}H NMR SQDQ Baba spectrum of **MIL-140C_1**. This experiment confirms the existence of two distinct chemical environments for the ligands and short contacts between them through the Hb and Hc protons. b) ^{1}H-^{13}C NMR HETCOR CPMAS spectrum of **MIL-140C_1**, allowing the assignment of all ^{1}H and ^{13}C NMR lines with respect to two distinct ligands (A and A' corresponding to site 2 and site 1, respectively).*

To gain further structural insights, **MIL-140C_1** was finally subjected to 2-D correlation experiments. ^{1}H-^{1}H SQ-DQ and ^{1}H-^{13}C HETCOR-CPMAS experiments confirmed the existence of two separate sets of resonances for phenolic OH groups and aromatic protons, associated with two distinct crystallographic sites occupied by the $BP(OH)_2DC$ ligand within the same solid, and allowed the full assignment of proton and carbon signals, as shown in Figure 5. Therefore, the two crystallographic sites are differentiated by NMR on the base of their preferential occupancy with respect to the nature of the framework ligand, and denoted as ligand A and A' in Figure 5.

In order to properly identify the sites associated with this preferential occupancy, all **MIL-140C_n** structures were refined from high resolution XRPD data (see Figures S6 and Table S4 for the final Rietveld plots and refinement parameters respectively). Indeed, whereas the structure of the smaller analogue MIL-140A (based on terephthalate) was experimentally solved and refined, the ones of MIL-140s obtained from longer linkers, and notably MIL-140C, were simply simulated based on experimental unit cell parameters.[29] Therefore, the structure of **MIL-140C_0** was first re-investigated. The whole powder pattern fitting without structural model showed that the previously reported unit cell parameters do not agree with the current pattern. Hence, the LP-Search indexing procedure was used to determine the correct unit cell in the *C*2/*c* space group. The structural model of the MIL-140A was then used as the starting point in the Rietveld refinement by replacing the terephthalate by the BPDC, which was treated as rigid body. As for MIL-140A, the BPDC ligands are located on two nonequivalent crystallographic sites in a 1 to 1 ratio. As shown in Figure 2, ligands in *site 1* are stacked parallel to each other with a distance between the aromatic rings of *ca.* 3.9 Å, while ligands in *site 2* are side-by-side with the shortest interatomic C•••C distance of 5.4 Å (C•••C distance between the carboxylic group equal to 7.8 Å). A 20° torsion angle is obtained between the benzene rings of the BPDC of *site 1* whereas the flatness of *site 2* is imposed by the inversion center. Attempts to lower the symmetry to the *Cc* space group were undertaken but did not significantly improve the refinement. Although phenyl rings are expected to be tilted in biphenyl moieties, the precise value of the torsion angle cannot be determined from our laboratory XRPD data (see discussion below).

Rietveld refinements of modified MIL-140C series were then undertaken in the *Cc* space group due to the lower symmetry of the organic linker. Moreover, tilt angle between phenyl rings was arbitrary fixed to 0 for both sites in the three compounds, knowing that no tilt was observed in the structure of the parent 2,2'-bipyridine-3,3'-diol-5,5'-diethyl dicarboxylic ester solved from single crystal X-ray diffraction.[38]

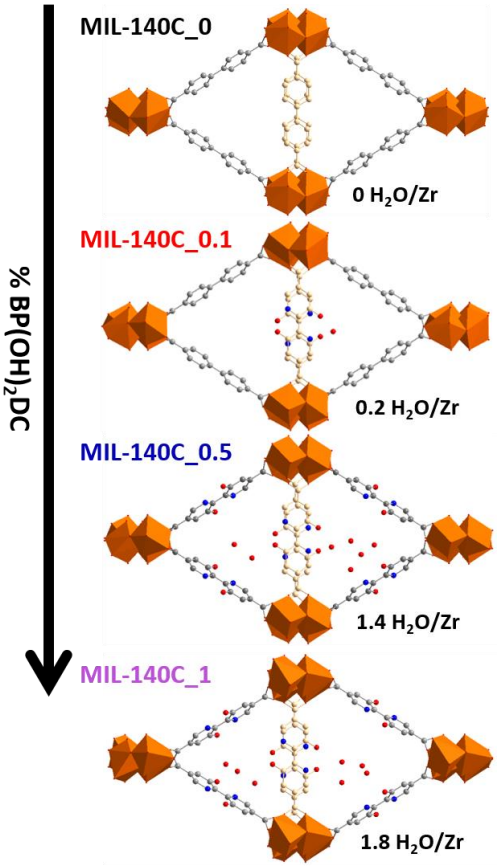

Figure 6. *Crystal structures of the* ***MIL-140C_n*** *series, view along the c axis.*

Figure 6 presents the comparison of crystal structures obtained for the whole series. For **MIL-140C_0.1**, the refinement revealed that the $BP(OH)_2DC$ ligands are all located in a single site, namely *site 1* (see Figure 2). This full agrees with the NMR experiments, which indicate the occurrence of a preferential site of occupancy for the $BP(OH)_2DC$ ligand (ligand A' on Figure 5), which ultimately corresponds to *site 1*. Such a preference is also found in the structure of **MIL-140C_0.5**, where ca. 3/4 of the $BP(OH)_2DC$ ligands are localized in the *site 1*, in rather good agreement with the value extracted from the NMR analysis (2/3).

As mentioned above, the value of the angle between the aromatic rings of the ligands cannot be accurately determined by XRPD. Moreover, rotation of these rings likely occurs in the solid state. Nevertheless, the presence of two strong OH•••N intramolecular hydrogen bonds is expected to favor a planar conformation for the $BP(OH)_2$ motif, whereas short intramolecular CH•••HC contacts favor the stabilization of a tilted geometry for the BPDC motif, as commonly observed in molecular compounds. This could explain why the $BP(OH)_2DC$ ligands are more easily accommodated in *site 1*, which is associated with shorter inter-ligand distances.

Porosity, hydrophilicity and stability

The porosity of the **MIL-140C_n** series was probed by nitrogen adsorption measurements at 77 K. As shown in Figure 7, all solids present a reversible type I isotherm, characteristic of microporous materials. The Brunauer–Emmett–Teller (BET) surface areas reached 790, 750 and 700 $m^2.g^{-1}$ for **MIL-140C_0.1**, **_0.5** and **_1**, respectively, compared to the expected value of 840 $m^2.g^{-1}$ for **MIL-140C_0**.[29] The pore volume followed the same trend (0.31, 0.27 and 0.25 $cm^3.g^{-1}$ for **MIL-140C_0.1**, **_0.5** and **_1**, respectively). The surface area and pore volume thus slightly decrease when the amount of $BP(OH)_2DC$ increases, as a consequence of the bulkier character of $BP(OH)_2DC$ compared to BPDC and the slight contraction of the unit-cell. The examination of the crystal structures with the Platon software indeed confirmed this trend (accessible void estimated to 42, 40 and 39 % for **MIL-140C_0.1**, **_0.5** and **_1**, respectively).

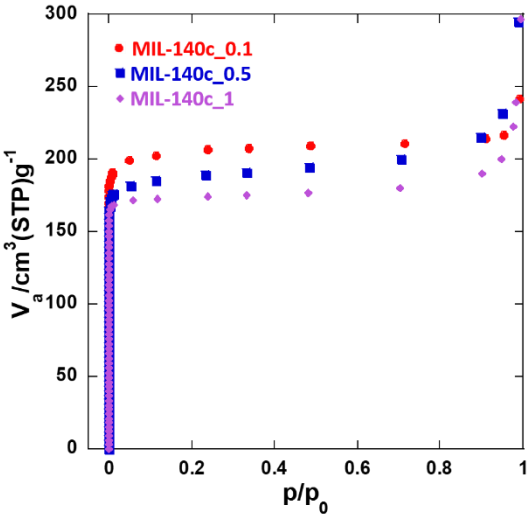

Figure 7. *N_2 adsorption measurements at 77 K of* ***MIL-140C_0.1****,* ***MIL-140C_0.5*** *and* ***MIL-140C_1****.*

Thermogravimetric analyses (TGA) were performed on all solids, both fresh and after two weeks of air exposure (Figures S7 and S8 respectively). For fresh **MIL-140C_0.5** and **MIL-140C_1**, the TG curves present a slight (~2.5 %) continuous loss of mass between 25 and ca. 250 °C, attributed to the removal of water from the pores, followed by a major weight loss starting at ca. 350 °C and associated with the combustion of the ligand. For **MIL-140C_0** and **MIL-140C_0.1**, the first weight loss is almost undetected (< 1%), in agreement with the hydrophobicity of the MIL-140s structures. After two weeks in air, no change is observed for **MIL-140C_0.1** (Figure S9). On the contrary, the TG curves of **MIL-140C_0.5** and **MIL-140C_1**, exhibit a more pronounced weight loss at low temperature of respectively 7.6 and 9.6%, corresponding to 1.7 and 2.2 water per Zr. This indicates that by increasing the amount of $BP(OH)_2DC$ ligand, the structure becomes more hydrophilic. Furthermore, in the case of **MIL-140C_0.5** and **MIL-140C_1**, the water removal occurred on a wide temperature range (20-170 °C), suggesting strong interactions between the water molecules and the framework. Indeed, it was possible to propose a plausible location of the water molecules from the structure determination. As shown in Figure 6, the refinement of the residual electronic density within the pores suggests the presence of 0.2 water molecule per Zr for **MIL-140_0.1,** while no water at all was observed for **MIL-140_0**. These values reached 1.4 and 1.8 for **MIL-140_0.5** and **MIL-140_1** respectively, with short intermolecular COH•••H_2O and H_2O•••H_2O distances, confirming the hydrophilic character of the $BP(OH)_2DC$ rich solids.

Knowing that MIL-140C is among the most stable Zr-based MOFs, the stability of the series towards water was evaluated.

First, for both hydrophobic (**MIL-140C_0.1**) and hydrophilic (**MIL-140C_1**) solids, no loss of crystallinity was observed after exposure to air for one month (Figure 8 and S9-S10). After ca. 4 months, while no change was still detected for **MIL-140C_0.1**, an obvious variation of the diffraction pattern occurred for **MIL-140C_1** (Figure S11). Note here that a similar behavior was already observed by D'Alessandro *et al.* when introducing large amount of 2,2'-bipyridine-5,5'-dicarboxylate within this structure type.[31] This effect is clearly related to the presence of water, since **MIL-140C_1** stored in dry atmosphere remains unaffected (see Figure S12). The stability was finally evaluated after suspending the solids in water (1 mg.mL^{-1}) for one week. Even under boiling conditions, no change was noticed on the powder XRD pattern of **MIL-140C_0.1** (Figure 8d), confirming the high stability of the $BP(OH)_2DC$-poor solids. Concerning **MIL-140C_1**, it was found to be unaltered at room temperature (Figure S13), whereas under refluxing conditions, an almost complete transformation to a new crystalline phase is observed (Figure 8g). A closer look indicates that this new phase does not contain crystallized ZrO_2 (Figure S15) and is the one which started to form after a long exposure to ambient air (Figure S11). Moreover, the infrared spectra of **MIL-140C_1** before and after the transformation are almost identical (Figures S15), and do not present vibration bands characteristics of the formation of free carboxylic acid (~1700 cm^{-1}) as often observed upon degradation of MOFs. Hence, the resulting product is likely a new coordination compound. Previously, Bennett *et al.* followed the degradation of MIL-140C upon ball milling, and noticed a complete amorphization together with the formation of free carboxylic acid groups.[37] Here, the transformation pathway is markedly different. The indexation of the XRPD pattern of the final product converged to a triclinic unit cell [a = 4.012(8), b = 14.061(7), c = 15.376(5) Å, α = 111.06(3), β = 91.4(3) and γ = 94.0(4)°, V = 806(2) Å^3], with a satisfactory figure of merit (M_{20} = 27), confirmed by its full pattern matching (R_{wp} = 0.087, see Figure S15). The poor quality of the dataset precluded any deeper structural analysis. Nevertheless, nitrogen sorption measurements carried out at 77 K suggests that this solid presents a very limited accessible porosity (see Figure S17).

To summarize, while the chemical stability of MIL-140C is maintained in $BP(OH)_2DC$-poor solids (**MIL-140_0.1**), the $BP(OH)_2DC$ rich samples are less stable, and this instability is associated with the easier adsorption of water. Hence, one may conclude that the high stability of most MIL-140 solids then derives from their strong hydrophobic character rather than from the unique nature of the constitutive inorganic building unit.[29, 31] This is moreover in line with previous studies on less water stable M(II) carboxylate MOFs, which evidenced the interplay between hydrophobicity and water stability.[39-40]

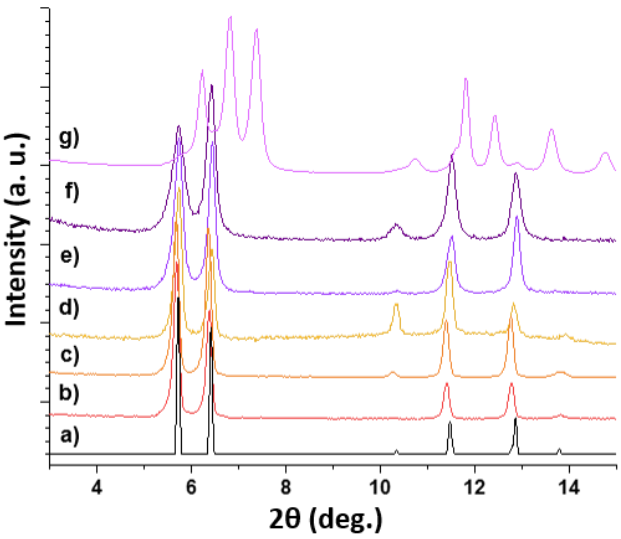

Figure 8. *Powder X-ray diffraction patterns of a)* ***MIL-140C_1*** *simulated from the crystal structure, b)* ***MIL-140C_0.1*** *as synthesized, c)* ***MIL-140C_0.1*** *after 1 month in air, d)* ***MIL-140C_0.1*** *after 1 week in boiling water, e)* ***MIL-140C_1*** *as synthesized, f)* ***MIL-140C_1*** *after 1 month in air, and g)* ***MIL-140C_1*** *after 1 week in boiling water.*

Photophysical properties

The optical properties of **MIL-140C_0.1**, **MIL-140C_0.5** and **MIL-140C_1** were investigated in the solid state and compared with the one of free $H_2BP(OH)_2DC$. As expected, upon excitation at 390 nm, all **MIL-140C-n** solids present a yellow emission characteristic to the ESIPT fluorescence of the ligand, while the **MIL140C_0** only shows a weak blue fluorescence emission (Figure 9). A slight blueshift is observed when moving from the free ligand to **MIL-140C_1** (emission centered at 562 and 550 nm respectively).

The fluorescent quantum yield of the whole series was also evaluated, and the resulting values are summarized in Table 1. All these compounds exhibit a high quantum yield (> 15%), of the same order of magnitude as the free ligand. The maximum value (35%) is obtained for **MIL-140C_0.1**, likely because the high level of dilution of the $BP(OH)_2DC$ emitter in the framework prevents the intermolecular quenching (see below).

Table 1. Fluorescent quantum yield of the title solids.

	λ_{ex} / nm	λ_{em} /nm	Φ
$BP(OH)_2DC$	390	562	0.29
MIL-140c_0.1	390	539	0.35
MIL-140c_0.5	390	547	0.27
MIL-140c_1	390	550	0.17

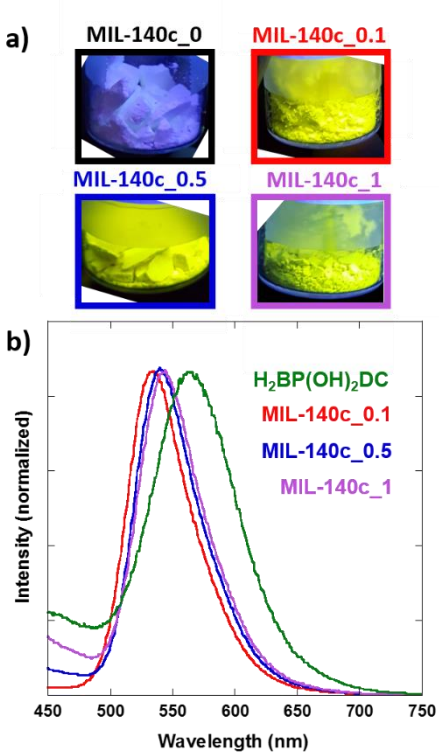

Figure 9. *a) Pictures of* ***MIL-140C_0***, ***_0.1***, ***_0.5*** *and* ***_1*** *under UV light at 365 nm and b) emission spectra of $H_2BP(OH)_2DC$ (green),* ***MIL-140C_0.1*** *(red),* ***_0.5*** *(blue) and* ***_1*** *(purple) after excitation at 390 nm.*

Time-resolved fluorescence emission was also studied for **MIL-140C_0.1**, **MIL-140C_0.5** and **MIL-140C_1** and compared with the solid molecular precursor $H_2BP(OH)_2DC$. Fluorescence decays were recorded at three emissions wavelengths (510, 530 and 580 nm, see Table S5). For all **MIL-140C_n** derivatives, the resulting decays could be satisfactorily fitted using a three-exponential model with three decay times (0.88, 3.16 and 4.79 ns). By comparison, the decays of the $H_2BP(OH)_2DC$ precursor could be fitted with a three exponentials model with decay times of 0.60, 2.60 and 5.11 ns (Table S6). While these decay times cannot be directly attributed to distinct crystallographic environments for the $BP(OH)_2DC$ ligand, we can note that in all cases, the long decay time is very close to the fluorescence lifetime measured for the diester precursor $BP(OH)_2(COOEt)_2$ in dichloromethane (4.64 ns).[38] For a given solid, the relative contributions of the three decay times to the overall fluorescence only slightly vary with the emission wavelength. This indicates that there are no excited-state processes such as excimers formation or resonance energy transfer occurring in these solids. The comparison of the three **MIL-140C_n** derivatives at a given emission wavelength shows that the higher the substitution rate the shorter the average fluorescence decay time (see Table S5). At high doping rates, there is apparition of some Aggregation Caused Quenching (ACQ), that could be due to stacking interactions between $BP(OH)_2DC$ ligands, while at low doping rate $BP(OH)_2DC$ ligands are diluted with BPDC ligands which limits the quenching. As a consequence, using low doping rate appears as an efficient strategy to limit ACQ.

Further experiments were conducted to evaluate the sensitivity of the emission of the most stable solids (**MIL-140C_0.1** and **MIL-140C_0.5**) towards pH variation. All experiments were carried out in very dilute conditions (5.10^{-6} mol.L-1, corresponding to ca. 2 mg of MOF per liter of water) to prevent reabsorption of the emitted fluorescence. The emission properties of a solution of ligand were first investigated (Figure S19). Upon increasing the pH from 4 to 8, the emission peak centered at ca. 500-510 nm is only slightly blue shifted, whereas as soon as pH 8-9 is reached, this peak vanishes and a new peak centered at 450-460 nm appears. While the first emission peak is attributed to the ESIPT process (see Figure 1), the second one, considering the pKa of the phenol group (~9) is associated to a partially deprotonated form of the dienol motif and thus a different electronic transition. For the MOFs in suspension (Figure S20), similar behaviors occur: a first emission peak centered at ~550 nm is visible in acidic medium, while a new band centered at 460 nm, this time of higher intensity, appears above pH 9. Nevertheless the increase of the pH above ~7 is also accompanied with a dissolution of the MOFs, in line with previous stability studies, which showed that under very dilute conditions, MOFs are usually unstable once pH reaches a higher value than the pKa of the binding group (here carboxylate).[41-42] Hence, while the sensitivity of the emission properties of the ligand makes it appealing for the detection of slight modifications of the pH in the 8-10 range, this range does not match with the stability range of the MOFs.

CONCLUSION

We reported here a series of Zr(IV)-based MOF series built up from an ESIPT-type fluorescent ligand. All these solids belong to the MIL-140 structure-type, and were found to combine a significant microporosity (S_{BET} > 700 $m^2.g^{-1}$) together with a high luminescent quantum yield (> 15%). These solids were found to be more hydrophilic than the pristine MIL-140C, and, as a consequence, less stable towards water. Nevertheless, by playing with the rate of ligand substitution, as exemplified with **MIL-140C_0.1**, it was possible to combine a good chemical stability with an optimized quantum yield (35%). Such solids thus appear of potential interest *e.g.* as emitters in light emitting devices or for optical detection in aqueous medium under proper pH conditions.

ASSOCIATED CONTENT

Supporting Information. Detailed synthetic conditions, elemental analyses, XRPD data, TG analyses, IR spectra, ^{13}C NMR spectra, fluorescence decay analysis. This material is available free of charge via the Internet at http://pubs.acs.org. Crystallographic data are available through the Cambridge Structural Database (CCDC 1895855-1895858).

AUTHOR INFORMATION

Corresponding Author

* E-mail address: virgile.trannoy@cnrs-imn.fr, pei.yu@u-psud.fr, thomas.devic@cnrs-imn.fr.

Author Contributions

V.T., A.L. and P.Y. took care of the synthesis and characterization of the fluorescent ligand; V.T., C.L., C.R.M. and T.D. were involved in the synthesis and characterization of the MOFs, N.G. conducted the PXRD analysis, M.H. conducted the NMR experiments; V.T., C.A. and G.C. were in charge of the optical studies. The manuscript was written through contributions of all authors.

Funding Sources

This work was supported by a public grant overseen by the French National Research Agency (ANR) as part of the "Inves-tissements d'Avenir" Program no. CHARMMMAT ANR-11-LABX-0039.

ACKNOWLEDGMENT

We acknowledge the labex CHARMMMAT (ANR-11-LABEX-0039) for the postdoctoral fellowships of Virgile Trannoy. Arnaud Brosseau (PPSM) is gratefully acknowledged for his help with the time-resolved fluorescence measurements.

REFERENCES

1. Allendorf, M. D.; Bauer, C. A.; Bhakta, R. K.; Houk, R. J. T., Luminescent metal-organic frameworks. *Chem. Soc. Rev.* **2009,** *38*, 1330-1352.
2. Lustig, W. P.; Mukherjee, S.; Rudd, N. D.; Desai, A. V.; Li, J.; Ghosh, S. K., Metal-organic frameworks: functional luminescent and photonic materials for sensing applications. *Chem. Soc. Rev.* **2017,** *46*, 3242-3285.
3. Zhang, Y.; Yuan, S.; Day, G.; Wang, X.; Yang, X.; Zhou, H.-C., Luminescent sensors based on metal-organic frameworks. *Coord. Chem. Rev.* **2018,** *354*, 28-45.
4. Cui, Y.; Yue, Y.; Qian, G.; Chen, B., Luminescent Functional Metal–Organic Frameworks. *Chem. Rev.* **2012,** *112*, 1126-1162.
5. Liu, D.; Lu, K.; Poon, C.; Lin, W., Metal–Organic Frameworks as Sensory Materials and Imaging Agents. *Inorg. Chem.* **2014,** *53*, 1916-1924.
6. Mahata, P.; Mondal, S. K.; Singha, D. K.; Majee, P., Luminescent rare-earth-based MOFs as optical sensors. *Dalton Trans.* **2017,** *46*, 301-328.
7. Müller-Buschbaum, K.; Beuerle, F.; Feldmann, C., MOF based luminescence tuning and chemical/physical sensing. *Microporous Mesoporous Mater.* **2015,** *216*, 171-199.
8. Monguzzi, A.; Ballabio, M.; Yanai, N.; Kimizuka, N.; Fazzi, D.; Campione, M.; Meinardi, F., Highly Fluorescent Metal–Organic-Framework Nanocomposites for Photonic Applications. *Nano Lett.* **2018,** *18*, 528-534.
9. Liu, X.-G.; Tao, C.-L.; Yu, H.-Q.; Chen, B.; Liu, Z.; Zhu, G.-P.; Zhao, Z.; Shen, L.; Tang, B. Z., A new luminescent metal-organic framework based on dicarboxyl-substituted tetraphenylethene for efficient detection of nitro-containing explosives and antibiotics in aqueous media. *J. Mater. Chem. C* **2018,** *6*, 2983-2988.
10. Li, Q.-Y.; Ma, Z.; Zhang, W.-Q.; Xu, J.-L.; Wei, W.; Lu, H.; Zhao, X.; Wang, X.-J., AIE-active tetraphenylethene functionalized metal-organic framework for selective detection of nitroaromatic explosives and organic photocatalysis. *Chem. Commun.* **2016,** *52*, 11284-11287.
11. Deng, Y.; Chen, N.; Li, Q.; Wu, X.; Huang, X.; Lin, Z.; Zhao, Y., Highly Fluorescent Metal–Organic Frameworks Based on a Benzene-Cored Tetraphenylethene Derivative with the Ability To Detect 2,4,6-Trinitrophenol in Water. *Crystal Growth Des.* **2017,** *17*, 3170-3177.
12. Eon, K. J.; Young, P. S., Advanced Organic Optoelectronic Materials: Harnessing Excited-State Intramolecular Proton Transfer (ESIPT) Process. *Adv. Mater.* **2011,** *23*, 3615-3642.
13. Padalkar, V. S.; Seki, S., Excited-state intramolecular proton-transfer (ESIPT)-inspired solid state emitters. *Chem. Soc. Rev.* **2016,** *45*, 169-202.
14. Jayaramulu, K.; Kanoo, P.; George, S. J.; Maji, T. K., Tunable emission from a porous metal-organic framework by employing an excited-state intramolecular proton transfer responsive ligand. *Chem. Commun.* **2010,** *46*, 7906-7908.
15. Jayaramulu, K.; Narayanan, R. P.; George, S. J.; Maji, T. K., Luminescent Microporous Metal–Organic Framework with Functional Lewis Basic Sites on the Pore Surface: Specific Sensing and Removal of Metal Ions. *Inorg. Chem.* **2012,** *51*, 10089-10091.
16. Shustova, N. B.; Cozzolino, A. F.; Reineke, S.; Baldo, M.; Dincă, M., Selective Turn-On Ammonia Sensing Enabled by High-Temperature Fluorescence in Metal–Organic Frameworks with Open Metal Sites. *J. Am. Chem. Soc.* **2013,** *135*, 13326-13329.
17. Douvali, A.; Tsipis, A. C.; Eliseeva, S. V.; Petoud, S.; Papaefstathiou, G. S.; Malliakas, C. D.; Papadas, I.; Armatas, G. S.; Margiolaki, I.; Kanatzidis, M. G.; Lazarides, T.; Manos, M. J., Turn-On Luminescence Sensing and Real-Time Detection of Traces of Water in Organic Solvents by a Flexible Metal–Organic Framework. *Angew. Chem. Int. Ed.* **2015,** *54*, 1651-1656.
18. Douvali, A.; Papaefstathiou, G. S.; Gullo, M. P.; Barbieri, A.; Tsipis, A. C.; Malliakas, C. D.; Kanatzidis, M. G.; Papadas, I.; Armatas, G. S.; Hatzidimitriou, A. G.; Lazarides, T.; Manos, M. J., Alkaline Earth Metal Ion/Dihydroxy–Terephthalate MOFs: Structural Diversity and Unusual Luminescent Properties. *Inorg. Chem.* **2015,** *54*, 5813-5826.
19. Chen, L.; Ye, J.-W.; Wang, H.-P.; Pan, M.; Yin, S.-Y.; Wei, Z.-W.; Zhang, L.-Y.; Wu, K.; Fan, Y.-N.; Su, C.-Y., Ultrafast water sensing and thermal imaging by a metal-organic framework with switchable luminescence. *Nature Commun.* **2017,** *8*, 15985.
20. Pournara, A. D.; Douvali, A.; Diamantis, S.; Papaefstathiou, G. S.; Hatzidimitriou, A. G.; Kaziannis, S.; Kosmidis, C.; Lazarides, T.; Manos, M. J., A new Cd^{2+}-dihydroxyterephthalate MOF: Synthesis, crystal structure and detailed photophysical studies. *Polyhedron* **2018,** *151*, 401-406.
21. Bhattacharya, B.; Halder, A.; Paul, L.; Chakrabarti, S.; Ghoshal, D., Eye-Catching Dual-Fluorescent Dynamic Metal–Organic Framework Senses Traces of Water: Experimental Findings and Theoretical Correlation. *Chem. Eur. J.* **2016,** *22*, 14998-15005.
22. Chen, L.; Zhang, H.; Pan, M.; Wei, Z.-W.; Wang, H.-P.; Fan, Y.-N.; Su, C.-Y., An Efficient Visible and Near-Infrared (NIR) Emitting SmIII Metal–Organic Framework (Sm-MOF) Sensitized by Excited-State Intramolecular Proton Transfer (ESIPT) Ligand. *Chem. Asian J.* **2016,** *11*, 1765-1769.
23. Li, Y.-P.; Li, S.-N.; Jiang, Y.-C.; Hu, M.-C.; Zhai, Q.-G., A semiconductor and fluorescence dual-mode room-temperature ammonia sensor achieved by decorating hydroquinone into a metal–organic framework. *Chem. Commun.* **2018,** *54*, 9789-9792.
24. Low, J. J.; Benin, A. I.; Jakubczak, P.; Abrahamian, J. F.; Faheem, S. A.; Willis, R. R., Virtual High Throughput Screening Confirmed Experimentally: Porous Coordination Polymer Hydration. *J. Am. Chem. Soc.* **2009,** *131*, 15834-15842.
25. Kim, M.; Cohen, S. M., Discovery, development, and functionalization of Zr(iv)-based metal-organic frameworks. *CrystEngComm* **2012,** *14*, 4096-4104.
26. Devic, T.; Serre, C., High valence 3p and transition metal based MOFs. *Chem. Soc. Rev.* **2014,** *43*, 6097-6115.
27. Bai, Y.; Dou, Y.; Xie, L.-H.; Rutledge, W.; Li, J.-R.; Zhou, H.-C., Zr-based metal–organic frameworks: design, synthesis, structure, and applications. *Chem. Soc. Rev.* **2016,** *45*, 2327-2367.
28. Cavka, J. H.; Jakobsen, S.; Olsbye, U.; Guillou, N.; Lamberti, C.; Bordiga, S.; Lillerud, K. P., A New Zirconium Inorganic Building Brick Forming Metal Organic Frameworks with Exceptional Stability. *J. Am. Chem. Soc.* **2008,** *130*, 13850-13851.
29. Guillerm, V.; Ragon, F.; Dan-Hardi, M.; Devic, T.; Vishnuvarthan, M.; Campo, B.; Vimont, A.; Clet, G.; Yang, Q.; Maurin, G.; Férey, G.; Vittadini, A.; Gross, S.; Serre, C., A Series of Isoreticular, Highly Stable, Porous Zirconium Oxide Based Metal–Organic Frameworks. *Angew. Chem. Int. Ed.* **2012,** *51*, 9267-9271.
30. Liang, W.; D'Alessandro, D. M., Microwave-assisted solvothermal synthesis of zirconium oxide based metal–organic frameworks. *Chem. Commun.* **2013,** *49*, 3706-3708.
31. Liang, W.; Babarao, R.; Church, T. L.; D'Alessandro, D. M., Tuning the cavities of zirconium-based MIL-140 frameworks to modulate CO2 adsorption. *Chem. Commun.* **2015,** *51*, 11286-11289.

32. Liang, W.; Babarao, R.; D'Alessandro, D. M., Microwave-Assisted Solvothermal Synthesis and Optical Properties of Tagged MIL-140A Metal–Organic Frameworks. *Inorg. Chem.* **2013,** *52*, 12878-12880.
33. Van de Voorde, B.; Damasceno Borges, D.; Vermoortele, F.; Wouters, R.; Bozbiyik, B.; Denayer, J.; Taulelle, F.; Martineau, C.; Serre, C.; Maurin, G.; De Vos, D., Isolation of Renewable Phenolics by Adsorption on Ultrastable Hydrophobic MIL-140 Metal–Organic Frameworks. *ChemSusChem* **2015,** *8*, 3159-3166.
34. *Topas V5: General Profile and Structure Analysis Software for Powder Diffraction Data*, Bruker AXS Ltd: 2014.
35. Salomon, W.; Roch-Marchal, C.; Mialane, P.; Rouschmeyer, P.; Serre, C.; Haouas, M.; Taulelle, F.; Yang, S.; Ruhlmann, L.; Dolbecq, A., Immobilization of polyoxometalates in the Zr-based metal organic framework UiO-67. *Chem. Commun.* **2015,** *51*, 2972-2975.
36. Lawrence, M. C.; Schneider, C.; Katz, M. J., Determining the structural stability of UiO-67 with respect to time: a solid-state NMR investigation. *Chem. Commun.* **2016,** *52*, 4971-4974.
37. Bennett, T. D.; Todorova, T. K.; Baxter, E. F.; Reid, D. G.; Gervais, C.; Bueken, B.; Van de Voorde, B.; De Vos, D.; Keen, D. A.; Mellot-Draznieks, C., Connecting defects and amorphization in UiO-66 and MIL-140 metal–organic frameworks: a combined experimental and computational study. *Phys. Chem. Chem. Phys.* **2016,** *18*, 2192-2201.
38. Yu, P.; Trannoy, V.; Leaustic, A.; Guillot, R.; Geffroy, B.; Allain, C.; Clavier, G., *manuscript in preparation.*
39. Jasuja, H.; Huang, Y.-g.; Walton, K. S., Adjusting the Stability of Metal–Organic Frameworks under Humid Conditions by Ligand Functionalization. *Langmuir* **2012,** *28*, 16874-16880.
40. Jasuja, H.; Burtch, N. C.; Huang, Y.-g.; Cai, Y.; Walton, K. S., Kinetic Water Stability of an Isostructural Family of Zinc-Based Pillared Metal–Organic Frameworks. *Langmuir* **2013,** *29*, 633-642.
41. Cunha, D.; Ben Yahia, M.; Hall, S.; Miller, S. R.; Chevreau, H.; Elkaïm, E.; Maurin, G.; Horcajada, P.; Serre, C., Rationale of Drug Encapsulation and Release from Biocompatible Porous Metal–Organic Frameworks. *Chem.Mater.* **2013,** *25*, 2767-2776.
42. Bellido, E.; Guillevic, M.; Hidalgo, T.; Santander-Ortega, M. J.; Serre, C.; Horcajada, P., Understanding the Colloidal Stability of the Mesoporous MIL-100(Fe) Nanoparticles in Physiological Media. *Langmuir* **2014,** *30*, 5911-5920.